Revisiting 3D Reconstruction Kernels as Low-Pass Filters

Supplementary Material

A. Jinc Kernel

In this section, we perform detailed derivation of Jinc kernel proposed in Section 4.1.

A.1. Frequency Domain Definition

The ideal low-pass filter (ILPF) in three dimensions is a theoretical construct used in signal processing for multi-dimensional signals, such as volumetric data or 3D images. Its frequency domain transfer function is a spherical indicator function, allowing frequency components within a cutoff radius to pass unattenuated while blocking higher frequencies. The spatial domain response, or impulse response, is obtained via the inverse Fourier transform. We use the following conventions:

$$H(\mathbf{f}) = \iiint h(\mathbf{r}) e^{-j2\pi \mathbf{f}\cdot\mathbf{r}}\, dx\, dy\, dz, \tag{1}$$

$$h(\mathbf{r}) = \iiint H(\mathbf{f}) e^{j2\pi \mathbf{f}\cdot\mathbf{r}}\, df_x\, df_y\, df_z, \tag{2}$$

where $j = \sqrt{-1}$.

The transfer function of the 3D ideal low-pass filter with cutoff frequency f_c is:

$$H(\mathbf{f}) = \begin{cases} 1, & \|\mathbf{f}\| \le f_c, \\ 0, & \|\mathbf{f}\| > f_c, \end{cases} \tag{3}$$

where $\|\mathbf{f}\| = \sqrt{f_x^2 + f_y^2 + f_z^2}$. This defines a spherical passband in the frequency domain.

A.2. Derivation of the Spatial Response

Due to the radial symmetry of $H(\mathbf{f})$, the spatial response $h(\mathbf{r})$ depends only on $r = \|\mathbf{r}\| = \sqrt{x^2 + y^2 + z^2}$. We compute $h(r)$ using spherical coordinates in the frequency domain. The inverse Fourier transform becomes:

$$\begin{aligned} h(r) &= \int_0^{f_c}\int_0^{\pi}\int_0^{2\pi} e^{j2\pi f r\cos\theta} f^2 \sin\theta\, d\phi\, d\theta\, df, \\ &= 2\pi \int_0^{f_c} f^2 \int_0^{\pi} e^{j2\pi f r\cos\theta} \sin\theta\, d\theta\, df, \\ &= 2\pi \int_0^{f_c} f^2 \cdot \frac{2\sin(2\pi f r)}{2\pi f r}\, df, \\ &= \frac{4\pi}{2\pi r}\int_0^{f_c} f^2 \cdot \frac{\sin(2\pi f r)}{f}\, df, \\ &= \frac{2}{r}\int_0^{f_c} f \sin(2\pi f r)\, df, \\ &= \frac{1}{2\pi^2 r^3}\left[\sin(2\pi f_c r) - 2\pi f_c r\cos(2\pi f_c r)\right]. \end{aligned} \tag{4}$$

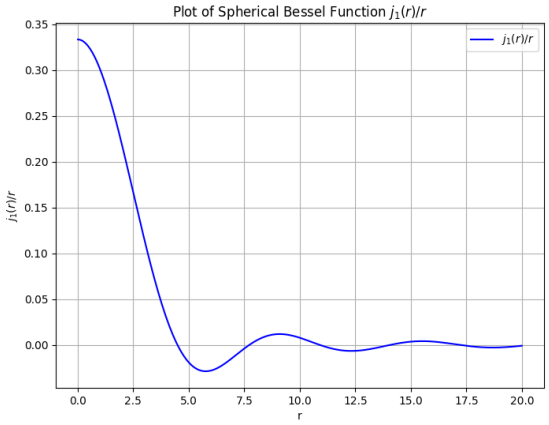

Figure 1. The sketch map of half of the ILPF.

The spherical Bessel function of the first kind $j_1(\alpha)$ is given as:

$$j_1(\alpha) = \frac{\sin\alpha - \alpha\cos\alpha}{\alpha^2}. \tag{5}$$

So, we have:

$$h(r) = \frac{1}{2\pi^2 r^3}\cdot(2\pi f_c r)^2 j_1(2\pi f_c r) = \frac{2f_c^2}{r} j_1(2\pi f_c r).$$

The curve of $j_1(r)/r$ is visualized in Figure 1

A.3. Anisotropy ILPF

We have discussed about the isotropy ILPF above. Now we introduce the definition of the anisotropy ILPF:

$$h(\boldsymbol{x}) = \frac{j_1(\sqrt{(\boldsymbol{x}-\boldsymbol{\mu})^\top \Sigma^{-1}(\boldsymbol{x}-\boldsymbol{\mu})})}{\sqrt{(\boldsymbol{x}-\boldsymbol{\mu})^\top \Sigma^{-1}(\boldsymbol{x}-\boldsymbol{\mu})}}, \tag{6}$$

where $\boldsymbol{\mu}$ is the center postion of ILPF and $\Sigma = RSS^\top R^\top$ is the covariance matrix. Here we ignore the outoff frequency, which can be absorbed into the scale matrix S.

B. Jinc Splatting

In this section, we perform detailed derivation for Jinc Splatting in Section 4.2.

B.1. Integration Along a Line

This section derives the integral of the spatial response of a three-dimensional ideal low-pass filter along an arbitrary straight line $\mathbf{x}(t) = \mathbf{a} + t\mathbf{b}$, where $\mathbf{a} = (a_x, a_y, a_z)$, $\mathbf{b} = (b_x, b_y, b_z)$, and $t \in (-\infty, \infty)$.

We need to compute:

$$
\begin{aligned}
I &= \int_{-\infty}^{\infty} h(\boldsymbol{x}(t))\, dt, \\
&= \int_{-\infty}^{\infty} \frac{j_1(\sqrt{(\boldsymbol{x}(t)-\boldsymbol{\mu})^\top \Sigma^{-1}(\boldsymbol{x}(t)-\boldsymbol{\mu})})}{\sqrt{(\boldsymbol{x}(t)-\boldsymbol{\mu})^\top \Sigma^{-1}(\boldsymbol{x}(t)-\boldsymbol{\mu})}}\, dt, \\
&= \int_{-\infty}^{\infty} \frac{j_1\left(\sqrt{((\boldsymbol{a}-\boldsymbol{\mu})+t\boldsymbol{b})^\top \Sigma^{-1}((\boldsymbol{a}-\boldsymbol{\mu})+t\boldsymbol{b})}\right)}{\sqrt{((\boldsymbol{a}-\boldsymbol{\mu})+t\boldsymbol{b})^\top \Sigma^{-1}((\boldsymbol{a}-\boldsymbol{\mu})+t\boldsymbol{b})}}\, dt.
\end{aligned}
$$

Since $\Sigma = RSS^\top R^\top$, we define $\boldsymbol{m} = S^{-1}R^{-1}(\boldsymbol{a}-\boldsymbol{\mu})$ and $\boldsymbol{n} = S^{-1}R^{-1}\boldsymbol{b}$. Thus, we have:

$$
\begin{aligned}
&((\boldsymbol{a}-\boldsymbol{\mu})+t\boldsymbol{b})^\top \Sigma^{-1}((\boldsymbol{a}-\boldsymbol{\mu})+t\boldsymbol{b}) \\
=&(\boldsymbol{m}+t\boldsymbol{n})^\top(\boldsymbol{m}+t\boldsymbol{n}), \\
=&\|\boldsymbol{m}\|^2 + 2t(\boldsymbol{m}\cdot\boldsymbol{n}) + t^2\|\boldsymbol{n}\|^2. \qquad (7)
\end{aligned}
$$

Substitute $s = t + \boldsymbol{m}\cdot\boldsymbol{n}/\|\boldsymbol{n}\|^2$, the integration transfers to:

$$
\begin{aligned}
I &= \int_{-\infty}^{\infty} \frac{j_1\left(\sqrt{((\boldsymbol{a}-\boldsymbol{\mu})+t\boldsymbol{b})^\top \Sigma^{-1}((\boldsymbol{a}-\boldsymbol{\mu})+t\boldsymbol{b})}\right)}{\sqrt{((\boldsymbol{a}-\boldsymbol{\mu})+t\boldsymbol{b})^\top \Sigma^{-1}((\boldsymbol{a}-\boldsymbol{\mu})+t\boldsymbol{b})}}\, dt, \\
&= \int_{-\infty}^{\infty} \frac{j_1\left(\sqrt{\|\boldsymbol{m}\|^2 + 2t(\boldsymbol{m}\cdot\boldsymbol{n}) + t^2\|\boldsymbol{n}\|^2}\right)}{\sqrt{\|\boldsymbol{m}\|^2 + 2t(\boldsymbol{m}\cdot\boldsymbol{n}) + t^2\|\boldsymbol{n}\|^2}}\, dt, \\
&= \int_{-\infty}^{\infty} \frac{j_1\left(\|\boldsymbol{n}\|\sqrt{s^2 + \frac{\|\boldsymbol{m}\times\boldsymbol{n}\|^2}{\|\boldsymbol{n}\|^4}}\right)}{\|\boldsymbol{n}\|\sqrt{s^2 + \frac{\|\boldsymbol{m}\times\boldsymbol{n}\|^2}{\|\boldsymbol{n}\|^4}}}\, ds, \\
&= \int_{-\infty}^{\infty} \frac{j_1\left(\frac{\|\boldsymbol{m}\times\boldsymbol{n}\|}{\|\boldsymbol{n}\|}\sqrt{v^2+1}\right)}{\|\boldsymbol{n}\|\sqrt{v^2+1}}\, dv, \\
&= \int_{-\infty}^{\infty} \frac{j_1\left(\alpha\sqrt{v^2+1}\right)}{\|\boldsymbol{n}\|\sqrt{v^2+1}}\, dv, \\
&= \frac{\pi J_1(\alpha)}{\|\boldsymbol{n}\|\alpha} \qquad (8)
\end{aligned}
$$

B.2. Gradient Backward Propagation

This section derives the backward propagation for Jinc Splatting in Section 4.2.4.

B.2.1. The Partial Derivative of I with respect to α

First, we have the differential of $j_1(x)$:

$$
j_1'(x) = j_0(x) - \frac{2}{x} j_1(x), \qquad (9)
$$

$$
j_0(x) = \frac{sin(x)}{x}, \quad j_1(x) = \frac{sin(x) - xcos(x)}{x^2}. \qquad (10)
$$

Thus:

$$
\begin{aligned}
\frac{\partial I}{\partial \alpha} &= \int_{-\infty}^{\infty} \frac{1}{\|\boldsymbol{n}\|\sqrt{v^2+1}} \frac{\partial j_1\left(\alpha\sqrt{v^2+1}\right)}{\partial \alpha}\, dv \\
&= \int_{-\infty}^{\infty} \frac{\partial j_1\left(\alpha\sqrt{v^2+1}\right)}{\|\boldsymbol{n}\|\partial\left(\alpha\sqrt{v^2+1}\right)}\, dv \\
&= \frac{1}{\|\boldsymbol{n}\|}\int_{-\infty}^{\infty} j_0\left(\alpha\sqrt{v^2+1}\right) - \frac{2j_1\left(\alpha\sqrt{v^2+1}\right)}{\alpha\sqrt{v^2+1}}\, dv \\
&= \frac{1}{\|\boldsymbol{n}\|}\left[\frac{\pi J_0(\alpha)}{\alpha} - \frac{2\pi J_1(\alpha)}{\alpha^2}\right]. \qquad (11)
\end{aligned}
$$

B.2.2. The Partial Derivative of α with respect to μ

The partial derivative of α with respect to μ can be formulated as:

$$
\begin{aligned}
\frac{\partial \alpha}{\partial \boldsymbol{\mu}} &= \frac{1}{2\alpha}\frac{\partial}{\partial \boldsymbol{\mu}}\left(\|\boldsymbol{m}\|^2 - \frac{(\boldsymbol{m}^\top\boldsymbol{n})^2}{\|\boldsymbol{n}\|^2}\right) \\
&= \frac{1}{2\alpha}\left(\frac{\partial(\boldsymbol{m}^\top\boldsymbol{m})}{\partial\boldsymbol{\mu}} - \frac{\partial}{\partial\boldsymbol{\mu}}\left(\frac{(\boldsymbol{m}^\top\boldsymbol{n})^2}{\|\boldsymbol{n}\|^2}\right)\right) \\
&= \frac{1}{2\alpha}\left(2\left(\frac{\partial\boldsymbol{m}}{\partial\boldsymbol{\mu}}\right)^\top\boldsymbol{m} - \frac{2(\boldsymbol{m}^\top\boldsymbol{n})}{\|\boldsymbol{n}\|^2}\left(\frac{\partial\boldsymbol{m}}{\partial\boldsymbol{\mu}}\right)^\top\boldsymbol{n}\right) \\
&= \frac{1}{2\alpha}\left(-2(\boldsymbol{S}^{-1}\boldsymbol{R}^{-1})^\top\boldsymbol{m} + \frac{2(\boldsymbol{m}^\top\boldsymbol{n})}{\|\boldsymbol{n}\|^2}(\boldsymbol{S}^{-1}\boldsymbol{R}^{-1})^\top\boldsymbol{n}\right) \\
&= \frac{1}{\alpha}\left(-(\boldsymbol{S}^{-1}\boldsymbol{R}^{-1})^\top\boldsymbol{m} + \frac{\boldsymbol{m}^\top\boldsymbol{n}}{\|\boldsymbol{n}\|^2}(\boldsymbol{S}^{-1}\boldsymbol{R}^{-1})^\top\boldsymbol{n}\right) \\
&= -\frac{1}{\alpha}(\boldsymbol{S}^{-1}\boldsymbol{R}^{-1})^\top\left(\boldsymbol{m} - \frac{\boldsymbol{m}^\top\boldsymbol{n}}{\|\boldsymbol{n}\|^2}\boldsymbol{n}\right) \\
&= -\frac{1}{\alpha}(\boldsymbol{R}\boldsymbol{S})^{-\top}\left(\boldsymbol{m} - \frac{\boldsymbol{m}^\top\boldsymbol{n}}{\|\boldsymbol{n}\|^2}\boldsymbol{n}\right). \qquad (12)
\end{aligned}
$$

B.2.3. The Partial Derivative of α with respect to Σ

The partial derivative of α with respect to Σ can be formulated as:

$$
\frac{\partial \alpha}{\partial \boldsymbol{\Sigma}} = \frac{1}{2\alpha}\left(\frac{\partial(\boldsymbol{m}^\top\boldsymbol{m})}{\partial\boldsymbol{\Sigma}} - \frac{\partial}{\partial\boldsymbol{\Sigma}}\left(\frac{(\boldsymbol{m}^\top\boldsymbol{n})^2}{\|\boldsymbol{n}\|^2}\right)\right). \qquad (13)
$$

We introduce the standard form of matrix differential in the numerator layout convention:

$$
df = \mathrm{tr}\left(\left(\frac{\partial f}{\partial \mathbf{X}}\right)^\top \mathbf{X}\right) \qquad (14)
$$

Similar to the partial derivative of α with respect to μ, given the standard form of matrix differential, we can get that:

$$
\begin{aligned}
\frac{\partial \alpha}{\partial \boldsymbol{\Sigma}} = \frac{\boldsymbol{\Sigma}^{-1}}{2\alpha(\boldsymbol{n}^\top\boldsymbol{\Sigma}^{-1}\boldsymbol{n})^2}\big(&-(\boldsymbol{n}^\top\boldsymbol{\Sigma}^{-1}\boldsymbol{n})^2\boldsymbol{m}\boldsymbol{m}^\top \qquad (15) \\
&+2(\boldsymbol{m}^\top\boldsymbol{\Sigma}^{-1}\boldsymbol{n})(\boldsymbol{n}^\top\boldsymbol{\Sigma}^{-1}\boldsymbol{n})\boldsymbol{n}\boldsymbol{m}^\top - (\boldsymbol{m}^\top\boldsymbol{\Sigma}^{-1}\boldsymbol{n})^2\boldsymbol{n}\boldsymbol{n}^\top\big)\,\boldsymbol{\Sigma}^{-1}.
\end{aligned}
$$

Table 1. **PSNR results for every scene in Mip-NeRF 360 [2] dataset**.

Method	bicycle	bonsai	counter	garden	kitchen	room	stump	average
Mip-NeRF [1]	24.37	33.46	29.55	26.98	32.23	31.64	26.40	29.23
3DHGS [7]	25.39	33.30	29.62	27.68	32.17	32.12	26.64	29.56
Scaffold-GS [8]	24.50	32.70	29.34	27.17	31.30	31.93	26.27	28.84
3DGS-MCMC [5]	26.15	32.88	29.51	28.16	32.27	32.48	27.80	29.89
3DGS [4]	**25.25**	31.98	28.70	**27.41**	30.32	30.63	26.55	28.69
Ours (3DGS)	25.17	**32.18**	**29.19**	**27.41**	**31.69**	**31.78**	**26.69**	**29.16**
SSS [9]	25.68	33.50	29.87	28.09	32.43	32.57	27.17	29.90
Ours (SSS)	**25.76**	**33.59**	**29.89**	**28.12**	**32.52**	**32.65**	**27.21**	**29.96**

Table 2. **SSIM results for every scene in Mip-NeRF 360 [2] dataset**.

Method	bicycle	bonsai	counter	garden	kitchen	room	stump	average
Mip-NeRF [1]	0.685	0.941	0.894	0.813	0.920	0.913	0.744	0.844
3DHGS [7]	0.768	0.950	0.909	0.868	0.930	0.921	0.770	0.873
Scaffold-GS [8]	0.705	0.946	0.914	0.842	0.928	0.925	0.784	0.848
3DGS-MCMC [5]	0.810	0.950	0.920	0.890	0.940	0.940	0.820	0.900
3DGS [4]	**0.771**	0.938	0.905	**0.868**	0.922	0.914	**0.775**	0.870
Ours (3DGS)	0.749	**0.946**	**0.915**	0.858	**0.933**	**0.928**	0.769	**0.871**
SSS [9]	**0.798**	**0.956**	**0.926**	0.882	0.939	0.938	**0.813**	**0.893**
Ours (SSS)	**0.798**	0.954	0.925	**0.883**	**0.940**	**0.939**	**0.813**	**0.893**

Table 3. **LPIPS results for every scene in Mip-NeRF 360 [2] dataset**.

Method	bicycle	bonsai	counter	garden	kitchen	room	stump	average
Mip-NeRF [1]	0.301	0.176	0.204	0.170	0.127	0.211	0.261	0.207
3DHGS [7]	0.202	0.180	0.201	0.104	0.125	0.220	0.215	0.178
Scaffold-GS [8]	0.306	0.185	0.191	0.146	0.126	0.202	0.284	0.220
3DGS-MCMC [5]	0.180	0.220	0.220	0.100	0.140	0.250	0.190	0.190
3DGS [4]	**0.205**	0.205	0.204	**0.103**	0.129	0.220	**0.210**	0.182
Ours (3DGS)	0.239	**0.177**	**0.181**	0.121	**0.115**	**0.193**	0.242	**0.181**
SSS [9]	**0.173**	0.151	0.156	**0.090**	0.104	0.167	**0.174**	0.145
Ours (SSS)	**0.173**	**0.141**	**0.155**	0.091	**0.103**	**0.166**	**0.174**	**0.143**

C. Additional Experimental Results

C.1. Detailed Results on Each Scene

We report detailed results on every scene in Mip-NeRF 360 [2], Tanks & Temples [6] and Deep Blending [3] for our modulated methods. We choose Mip-NeRF [1], 3DGS [4], Scaffold-GS [8], 3DHGS [7], 3DGS-MCMC [5] and SSS [9] as baselines.

As shown in Tabs. 1 to 6, in general, our modulation strategy outperforms both 3DGS [4] and SSS [9]. While the modulation strategy may not produce positive improvements in every scene, it delivers clear and consistent benefits in the majority cases.

C.2. Multi-Resolution Analysis

To further validate the correctness of our theoretical insights, we conduct a comprehensive multi-resolution evaluation. As the ideal jinc kernel exhibits slow spatial decay, a practical implementation inevitably requires spatial truncation. We therefore compare the truncated jinc kernel with the standard Gaussian kernel used in 3DGS by training both methods at the native resolution, followed by evaluation at the original resolution, as well as several downsampled resolutions. The experiment is conducted in Tanks & Temples [6].

The results shown in Tab. 7 demonstrate a consistent and theoretically aligned trend. At the native resolution, the truncated jinc kernel exhibits a slight performance drop relative to the Gaussian baseline, which is expected given the truncation. However, as the test resolution decreases,

Table 4. **PSNR results for every scene in Tanks & Temples [6] and Deep Blending [3].**

Method	Tanks & Temples			Deep Blending		
	train	truck	average	drjohnson	playroom	average
Mip-NeRF [1]	19.52	24.91	22.22	29.14	29.66	29.40
3DHGS [7]	22.95	26.04	24.49	29.32	30.20	29.76
Scaffold-GS [8]	22.15	25.77	23.96	29.80	30.62	30.21
3DGS-MCMC [5]	22.47	26.11	24.29	29.00	30.33	29.67
3DGS [4]	21.09	25.18	23.14	28.77	30.04	29.41
Ours (3DGS)	**22.18**	**25.54**	**23.86**	**29.41**	**30.26**	**29.84**
SSS [9]	23.32	26.41	24.87	29.66	30.47	30.07
Ours (SSS)	**23.47**	**26.42**	**24.95**	**29.71**	**30.62**	**30.17**

Table 5. **SSIM results for every scene in Tanks & Temples [6] and Deep Blending [3].**

Method	Tanks & Temples			Deep Blending		
	train	truck	average	drjohnson	playroom	average
Mip-NeRF [1]	0.660	0.857	0.759	0.901	0.900	0.901
3DHGS [7]	0.827	0.887	0.857	0.904	0.907	0.905
Scaffold-GS [8]	0.822	0.883	0.853	0.907	0.904	0.906
3DGS-MCMC [5]	0.830	0.890	0.860	0.890	0.900	0.890
3DGS [4]	0.802	0.879	0.841	0.899	0.906	0.903
Ours (3DGS)	**0.820**	**0.885**	**0.853**	**0.905**	**0.908**	**0.907**
SSS [9]	0.850	**0.897**	0.873	0.905	0.909	0.907
Ours (SSS)	**0.851**	**0.897**	**0.874**	**0.908**	**0.914**	**0.911**

Table 6. **LPIPS results for every scene in Tanks & Temples [6] and Deep Blending [3].**

Method	Tanks & Temples			Deep Blending		
	train	truck	average	drjohnson	playroom	average
Mip-NeRF [1]	0.354	0.159	0.257	0.237	0.252	0.245
3DHGS [7]	0.197	0.141	0.169	0.240	0.243	0.242
Scaffold-GS [8]	0.206	0.147	0.177	0.250	0.258	0.254
3DGS-MCMC [5]	0.240	0.140	0.190	0.330	0.310	0.320
3DGS [4]	0.218	0.148	0.183	0.244	0.241	0.243
Ours (3DGS)	**0.196**	**0.140**	**0.168**	**0.235**	**0.238**	**0.237**
SSS [9]	0.166	0.109	0.138	0.249	0.245	0.247
Ours (SSS)	**0.163**	**0.107**	**0.135**	**0.246**	**0.239**	**0.242**

Table 7. **Quantitative results with different resolutions in Tanks & Temples [6].**

Method	Full Resolution			1/2 Resolution			1/4 Resolution			1/8 Resolution		
	PSNR	SSIM	LPIPS	PSNR	SSIM	LPIPS	PSNR	SSIM	LPIPS	PSNR	SSIM	LPIPS
3DGS [4]	**23.14**	**0.841**	**0.183**	**22.16**	**0.838**	**0.136**	18.39	**0.686**	0.195	15.77	0.538	0.252
Jinc	22.55	0.824	0.186	21.98	0.812	0.143	**18.91**	0.673	**0.169**	**16.47**	**0.559**	**0.204**

the spatial support required for accurate reconstruction becomes correspondingly smaller. Under these conditions, the jinc kernel more faithfully preserves the frequency characteristics of the underlying signal and outperforms the Gaussian kernel. This resolution-dependent behavior provides additional evidence for the correctness of our theoretical analysis.

References

[1] Jonathan T. Barron, Ben Mildenhall, Matthew Tancik, Peter Hedman, Ricardo Martin-Brualla, and Pratul P. Srinivasan. Mip-nerf: A multiscale representation for anti-aliasing neural radiance fields. In *Proceedings of the IEEE/CVF International Conference on Computer Vision (ICCV)*, pages 5855–5864, 2021. 3, 4

[2] Jonathan T. Barron, Ben Mildenhall, Dor Verbin, Pratul P. Srinivasan, and Peter Hedman. Mip-nerf 360: Unbounded anti-aliased neural radiance fields. In *Proceedings of the IEEE/CVF Conference on Computer Vision and Pattern Recognition (CVPR)*, pages 5470–5479, 2022. 3

[3] Peter Hedman, Julien Philip, True Price, Jan-Michael Frahm, George Drettakis, and Gabriel Brostow. Deep blending for free-viewpoint image-based rendering. *ACM Transactions on Graphics (ToG)*, 37(6):1–15, 2018. 3, 4

[4] Bernhard Kerbl, Georgios Kopanas, Thomas Leimkühler, and George Drettakis. 3d gaussian splatting for real-time radiance field rendering, 2023. 3, 4

[5] Shakiba Kheradmand, Daniel Rebain, Gopal Sharma, Weiwei Sun, Yang-Che Tseng, Hossam Isack, Abhishek Kar, Andrea Tagliasacchi, and Kwang Moo Yi. 3d gaussian splatting as markov chain monte carlo. *Advances in Neural Information Processing Systems*, 37:80965–80986, 2024. 3, 4

[6] Arno Knapitsch, Jaesik Park, Qian-Yi Zhou, and Vladlen Koltun. Tanks and temples: Benchmarking large-scale scene reconstruction. *ACM Transactions on Graphics (ToG)*, 36(4): 1–13, 2017. 3, 4

[7] Haolin Li, Jinyang Liu, Mario Sznaier, and Octavia Camps. 3d-hgs: 3d half-gaussian splatting, 2025. 3, 4

[8] Tao Lu, Mulin Yu, Linning Xu, Yuanbo Xiangli, Limin Wang, Dahua Lin, and Bo Dai. Scaffold-gs: Structured 3d gaussians for view-adaptive rendering. In *Proceedings of the IEEE/CVF Conference on Computer Vision and Pattern Recognition*, pages 20654–20664, 2024. 3, 4

[9] Jialin Zhu, Jiangbei Yue, Feixiang He, and He Wang. 3d student splatting and scooping, 2025. 3, 4